Enzyme-mimicking single-atom FeN$_4$ sites for enhanced photo-Fenton-like reactions

Shiang Liu [a,1], Dan Liu [a,1], Yilang Sun [a], Peiyuan Xiao [a], Hongjun Lin [a], Jianrong Chen [a], Xi-Lin Wu [a,b,*], Xiaoguang Duan [b], Shaobin Wang [b]

[a] College of Geography and Environmental Science, Zhejiang Normal University, Jinhua 321004, China
[b] School of Chemical Engineering and Advanced Materials, The University of Adelaide, Adelaide, SA 5005, Australia
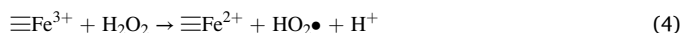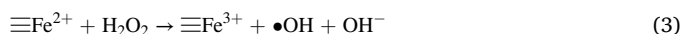
ARTICLE INFO

ABSTRACT

In this study, bio-inspired single-atom Fe (bio-SA-Fe) sites with pyrrole-type FeN$_4$ coordinations were embedded in graphitic carbon nitride (g-C$_3$N$_4$) via facile copolymerization approach. The bio-SA-Fe/g-C$_3$N$_4$ outperforms pure g-C$_3$N$_4$ and Fe-doped g-C$_3$N$_4$ (pyridine-type FeN$_4$ sites) in photo-Fenton-like reaction with a broad operating pH range (3−9), low consumption of H$_2$O$_2$, and remarkable stability and durability. Bader charge and differential charge distribution reveals the pyrrole-type FeN$_4$ sites are more conducive to charge distribution than the pyridine-type FeN$_4$ sites in g-C$_3$N$_4$, enabling faster electron transfer between the conjugated bio-SA-Fe sites and the g-C$_3$N$_4$ substrate. Density functional theory calculations further verified that the bio-SA-Fe sites are more stable and possess higher intrinsic activity for heterogeneous Fenton reaction than the pyridine-type FeN$_4$ sites in g-C$_3$N$_4$. This work provides important guidance for the rational design of robust bio-inspired single-atom catalysts for environmetal remediation and wide implications for other aqueous redox reactions.

1. Introduction

Purification techniques such as adsorption by activated carbon, membrane filtration (microfiltration, ultrafiltration, nanofiltration), and advanced oxidation processes (AOPs) have been applied for removing contaminants of emerging concerns (CECs) from wastewater [1]. AOPs are the rising stars of remediation technologies in recent years due to their simple operation, non-selectivity, fast kinetics, and high mineralization efficiency in the treatment of CECs [2]. AOPs are based on a strong oxidizing capacity of reactive oxygen species (ROS), such as hydroxyl radical (•OH) [3], singlet oxygen (^{1}O$_2$) [4], sulfate radical (SO$_4^{•-}$)[5] and superoxide radical (O$_2^{•-}$) [6]. Among the AOPs, Fenton reaction is one of the most promising techniques for the treatment of refractory wastewater, owing to the high redox potential of the •OH (E^0(•OH/H$_2$O) = 2.73 V) and its non-selectivity nature [7]. The classic Fenton reaction is driven by the redox cycle of Fe^{2+}/Fe^{3+} to generate •OH via the activation of H$_2$O$_2$ (Eqs. 1–2).

$$Fe^{2+} + H_2O_2 \rightarrow Fe^{3+} + •OH + OH^- \qquad (1)$$

$$Fe^{3+} + H_2O_2 \rightarrow Fe^{2+} + HO_2• + H^+ \qquad (2)$$
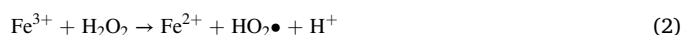
Fenton-like processes such as photo-Fenton and heterogeneous Fenton processes were also developed to intensify H$_2$O$_2$ activation. In the photo-Fenton processes, Fe^{2+} regeneration and H$_2$O$_2$ activation are simultaneously promoted by light irradiation. In contrast, in a heterogeneous Fenton process, H$_2$O$_2$ is decomposed by the iron species on the surface of solid catalysts (Eqs.3–4).

$$\equiv Fe^{2+} + H_2O_2 \rightarrow \equiv Fe^{3+} + •OH + OH^- \qquad (3)$$

$$\equiv Fe^{3+} + H_2O_2 \rightarrow \equiv Fe^{2+} + HO_2• + H^+ \qquad (4)$$

However, Fenton, photo-Fenton and heterogeneous Fenton systems usually suffer from slow regeneration of low-valence Fe^{2+}/$\equiv$Fe^{2+} species, a narrow working pH range, low utilization efficiency of H$_2$O$_2$, and poor stability of the catalysts in the oxidative environment [7–9]. These unresolved problems drive us to develop more active and robust Fenton catalysts with advanced strategies.

Atomically dispersed metal-based materials, namely single-atom catalysts (SACs), can bridge the gap between heterogeneous and homogeneous catalysis via drafting the single-atom (SA) configurations onto a solid support. SACs bear the features of easily recycling,

---

maximized metal utilization, unique catalytic activity and selectivity, and excellent durability [10–13]. In nature, many metalloenzymes have SA metal sites as the catalytic centers to drive biochemical reactions. For example, horseradish peroxidase and cytochrome P450 are natural oxidases and contain heme structure as the active center to catalyze the intracellular redox reactions [14]. SACs with similar atomic metal-organic coordination may inherit the characteristics of natural enzymes and exhibit respectful catalytic activity and selectivity. Moreover, the enzyme-like SACs supported on macroscale substrates hold the promises of low cost, structural robustness under harsh conditions, and feasibility for mass production. Bearing these in mind, the enzyme-like SACs may also be used as potential catalysts for environmental remediation.

Herein, inspired by the active center of natural enzymes, we designed and fabricated bio-inspired SACs by embedding the pyrrole-type Fe-N_4 single sites (SA-Fe) sites into a photoactive g-C_3N_4 substrate. The effects of light irradiation, solution pH, catalyst dosage and H_2O_2 concentration on the catalytic degradation of antibiotics by bio-SA-Fe/g-C_3N_4 mediated photo-Fenton-like reaction (PFLR) were systematically investigated. For the first time, we revealed that the pyrrole-type Fe-N_4 single sites in bio-SA-Fe/g-C_3N_4 possessed a much higher intrinsic activity in heterogeneous Fenton reactions than the previous reported pyridine-type FeN_4 sites in Fe-doped g-C_3N_4 (Fe/g-C_3N_4) by experimental and theoretical studies. The synergistic communications between pyrrole-type Fe-N_4 single sites and g-C_3N_4 substrates via the strong conjugated bonds secured the high catalytic performances and durability of bio-SA-Fe/g-C_3N_4 in PFLR, providing a robust and efficient Fenton-like system for the treatment of refractory wastewater.

2. Materials and methods

2.1. Catalyst Preparation and Characterizations

Chemicals used in this study are shown in **Text S1**, Supporting Information. Pristine g-C_3N_4 was synthesized by a one-step polymerization method, using urea as a precursor [15]. For the synthesis of bio-SA-Fe/g-C_3N_4, 8 g of urea and a certain amount of hemin were dissolved in 40 mL deionized water to form a homogeneous solution. The solution was continuously stirred for 30 min and dried at 70 °C. After that, the mixture was ground and heated to 550 °C at 3 °C/min and kept for 3 h in air. The resultant products were ground and washed with deionized water for several times to remove the impurities. The obtained product was denoted as Bio-SA-Fe/g-C_3N_4. Characterization techniques used in this study are provided in **Text S2**, Supporting Information.

2.2. Experimental procedure

Generally, desired amounts of catalysts and sulfamethoxazole (SMX) were added into 30 mL of water to form the reaction mixture. The initial solution pH was adjusted by 0.5 M HCl or 0.5 M NaOH. The obtained mixture was magnetically stirred for 120 min to achieve the adsorption-desorption equilibrium between the SMX and catalysts. Then, the catalytic oxidation processes were triggered by adding 60 μL of H_2O_2 into the above suspension with simultaneous light irradiation under a 300 W Xe lamp (PLS-SXE 300 C, Perfectlight, Beijing) with a piece of UV cutoff filter ($\lambda < 420$ nm). Samples were withdrawn at different time intervals, filtered through a 0.22 μm PTFE filter, and quenched with excessive methanol before analysis. The concentration of SMX was analyzed by high-performance liquid chromatography (HPLC, Shimadzu 20AV) with a C18 chromatographic column, a binary mobile phase (methanol: H_2O = 50: 50, v/v) at a flow rate of 0.8 mL/min and a UV/Vis detector at the detection wavelength of 265 nm. Degradation of other antibiotics (meropenem (MEM), metronidazole (MDZ), florfenicol (FFC), sulfisoxazole (SIZ) and ciprofloxacin (CIP)) was carried out using the same procedure as described above. The HPLC conditions for determination of the various antibiotics are listed in Table S1, Supporting Information.

For the reusability of bio-SA-Fe/g-C_3N_4, the recycled catalysts were separated, washed with deionized water three times and then dried in vacuum at 60 °C overnight for the next cycling test.

2.3. Computational details

All the spin-polarized density functional theory (DFT) calculations were carried out by using a Vienna Ab-initio Simulation Package (VASP) [16], with the projected augmented wave (PAW) method [17]. The exchange-correlation interactions were evaluated by using the Perdew-Burke-Ernzerhof (PBE) functional [18]. The plane-wave cut-off energy was set to be 450 eV. The convergence threshold was set to be 10^{-4} and 0.02 eV/Å for energy and force, respectively. A 15 Å vacuum layer was added to prevent the interaction between periodical images. The energy profiles for H_2O_2 activation by the Fe/g-C_3N_4 and bio-SA-Fe/g-C_3N_4 catalysts were evaluated by DFT calculations using a Gaussian 09 program (**Text S3**, Supporting Information.).

3. Results and discussion

3.1. Characterizations

As shown in Fig. S1, the enzyme-mimicking bio-SA-Fe/g-C_3N_4 catalyst was fabricated by copolymerization of urea and hemin at 550 °C [19]. The scanning electron microscopy (SEM) and transmission electron microscopy (TEM) images of pristine g-C_3N_4 and bio-SA-Fe/g-C_3N_4 illustrate their laminar structures with abundant nanopores (Fig. S2). Fe nanoparticles (NPs) were not observed from the high-resolution TEM (HRTEM) image of bio-SA-Fe/g-C_3N_4 (Fig. S3), suggesting the iron species were finely dispersed on the g-C_3N_4 substrate without aggregation. High-angle annular dark-field scanning TEM (HAADF-STEM) image (Fig. 1a) and the enlarged picture of a selected area (Fig. 1b) displayed a high density of tiny bright spots (marked with circles), corresponding to the atomically dispersed Fe atoms in the g-C_3N_4 substrate. TEM image (Fig. 1c) and the corresponding energy dispersive X-ray spectroscopy (EDX) mapping images (Fig. 1d-f) show the homogeneous distributions of C, N and Fe elements over bio-SA-Fe/g-C_3N_4, indicating the successful implantation of single-atom Fe sites into the g-C_3N_4 matrix.

From the X-ray diffraction (XRD) patterns of pristine g-C_3N_4 and bio-SA-Fe/g-C_3N_4 (Fig. 1g), the peaks at 13.1° and 27.3° were observed, assigned to the in-plane repeating tri-s-triazine ring structure and the typical graphitic layer stacking of g-C_3N_4, respectively [20]. Thus, bio-SA-Fe/g-C_3N_4 has the identical skeleton and crystal structure to the pristine g-C_3N_4. The survey spectra of X-ray photoelectron spectroscopy (XPS) show the coexistence of C, N and O elements in pure g-C_3N_4 and bio-SA-Fe/g-C_3N_4 (Fig. S4). The N 1 s XPS spectrum of bio-SA-Fe/g-C_3N_4 exhibits several N species at 398.4, 400.0 and 401.0 eV (Fig. 1h), which can be assigned to the sp^2-hybridized aromatic N (C=N-C, pyridinic N), tertiary N bonded with three carbon atoms (N-(C)$_3$) (or pyrrolic N), and the surface uncondensed amino groups (C-NH$_2$) in the heterocycles of g-C_3N_4, respectively [21,22]. As compared to pristine g-C_3N_4, the peak intensity of pyrrolic N was intensified for bio-SA-Fe/g-C_3N_4, attributing to the pyrrole-type Fe-N_x sites embedded in the g-C_3N_4 matrix. From the Fe 2p XPS spectrum of bio-SA-Fe/g-C_3N_4 (Fig. 1i), the peaks at 710.0 and 723.6 eV for Fe^{2+} and at 712.4 and 730.6 eV for Fe^{3+} can be observed [22]. The XPS peak for zero-valent Fe was not found, suggesting that Fe species were complexed by N atoms in the bio-SA-Fe/g-C_3N_4. The much higher peak intensities of Fe^{2+} species than those of Fe^{3+} species suggest the Fe(II)-N_x sites are dominant in bio-SA-Fe/g-C_3N_4, which are beneficial to the redox reaction of heterogeneous Fenton-like reactions.

The Fe K-edge X-ray absorption near edge structure (XANES) spectra were applied to verify the configuration of Fe sites in bio-SA-Fe/g-C_3N_4. As shown in Fig. 1j, the XANES spectra of bio-SA-Fe/g-C_3N_4 and iron phthalocyanine (FePc) are similar to each other, indicating their similar coordination structures and valence states. From the Fourier-
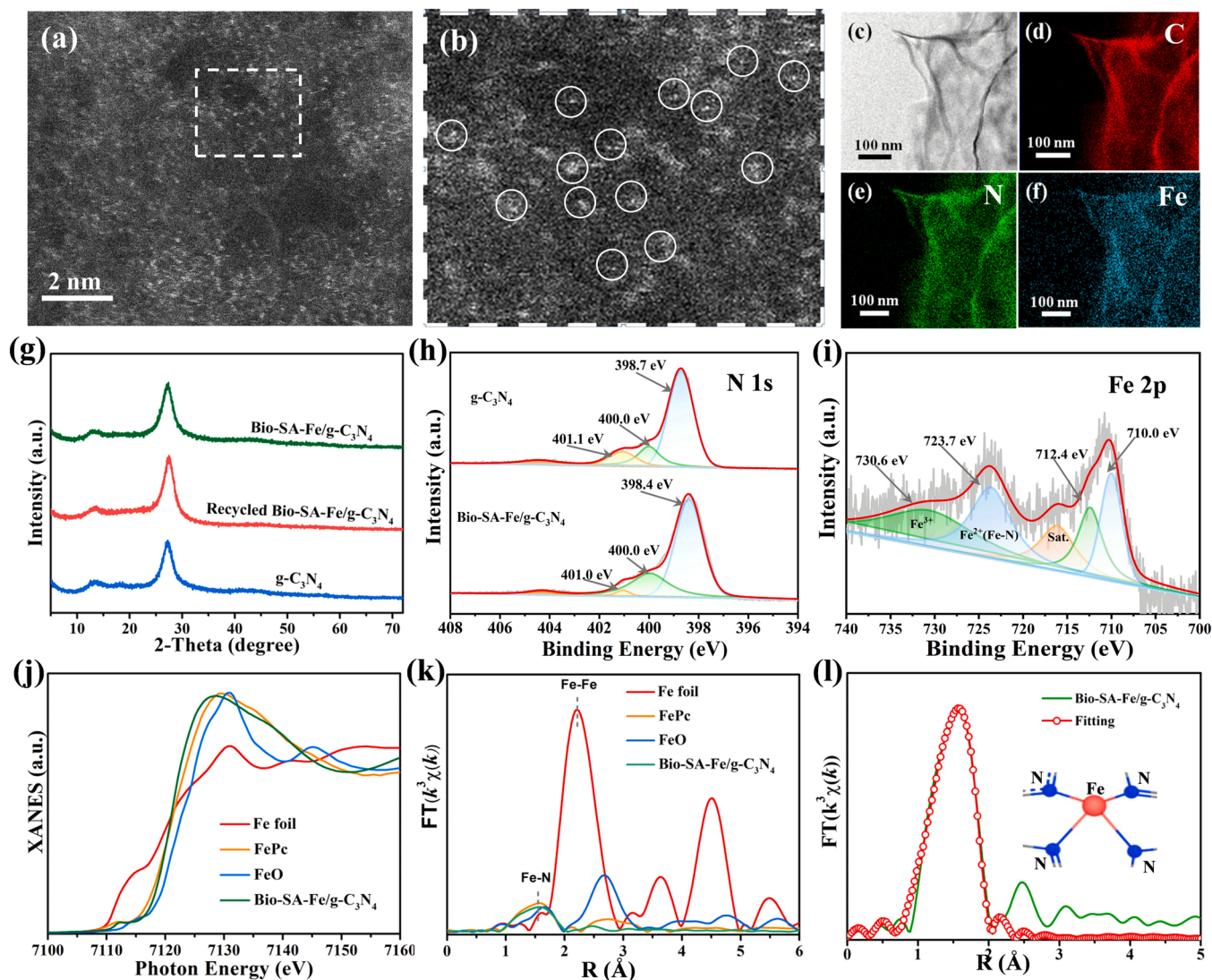
Fig. 1. (a) HAADF-STEM image, (b) the corresponding enlarged image of the selected area, (c) TEM image, and (d-f) the corresponding EDX mapping of bio-SA-Fe/g-C_3N_4. (g) XRD patterns of the samples. (h) High-resolution N 1s XPS spectra of the g-C_3N_4 and bio-SA-Fe/g-C_3N_4. (i) High-resolution Fe 2p XPS spectrum of bio-SA-Fe/g-C_3N_4. (j) XANES spectra and (k) Fourier transform (FT) XANES spectra at the Fe K-edge of bio-SA-Fe/g-C_3N_4, FeO, FePc and Fe foil. (f) EXAFS fitting curves of bio-SA-Fe/g-C_3N_4 at R-space.

transformed k^3-weighted extended X-ray absorption fine structure (FT-EXAFS) spectra (Fig. 1k), the bio-SA-Fe/g-C_3N_4 and FePc display one distinct peak at ~1.5 Å, which is assigned to the Fe-N first coordination shell [23,24]. The peak of the Fe-Fe coordination at ~2.2 Å was not observed, indicating the absence of Fe clusters or NPs in bio--SA-Fe/g-C_3N_4 [23]. In addition, the absence of Fe-Fe peak for the EXAFS oscillations in κ-space further confirms that the Fe atoms are solely co-ordinated by N atoms (Fe-N$_x$) in bio-SA-Fe/g-C_3N_4 (Fig. S5). The EXAFS fitting curve (Fig. 1l) and the related fitting parameters (Table S2) revealed that the coordination number of central Fe atoms is ~4.0 and the average bond length of Fe-N is 1.89 Å, which is shorter than the Fe-N bond (~2.09 Å) of the Fe-doped g-C_3N_4 [25]. The shorter Fe-N bond length in the bio-SA-Fe/g-C_3N_4 provides a stronger ligand field, result-ing in more stable Fe^{2+} species [26]. The stable and homogeneous dispersed pyrrole-type SA-Fe sites may provide abundant accessible catalytic centers to maximize the catalytic performances with high durability [27]. The Fe content in bio-SA-Fe/g-C_3N_4 was ~1.2 wt% determined by inductively coupled plasma-mass spectrometry (ICP-MS).

3.2. Catalytic performance of bio-SA-Fe/g-C_3N_4

Degradation of SMX by the bio-SA-Fe/g-C_3N_4 catalyst was system-atically studied. As shown in Fig. S6, the kinetics of SMX degradation slowed down gradually with increased solution pH from 3 to 11, sug-gesting that heterogeneous PFLR was favored at acidic conditions. This may be attributed to the decreased oxidation potential of •OH at increased pH values (2.65–2.80 V at pH 3 and 1.90 V at pH 7.0) [28,29]. The removal efficiencies of SMX reached ~100% in a pH range of 3–6, and they maintained as ~97%, 94% and 90% at pHs of 7, 8, and 9, respectively (Fig. 2a). This broad pH range overcomes the limitations in traditional Fenton systems, demonstrating the great advantage of bio--SA-Fe/g-C_3N_4 mediated PFLR in practical applications. Benefiting from the synergistic effects of photocatalysis and heterogeneous Fenton re-action in the bio-SA-Fe/g-C_3N_4 +H_2O_2 +Vis system, the consumption of H_2O_2 is minimized to 20.0 mmol/L (Fig. S7a). The degradation effi-ciency gradually climbed up with the increased catalyst dosage from 0.1 to 0.3 g/L (Fig. S7b). The increased amount of the catalyst will provide more exposed active sites for both photo- and heterogeneous catalytic processes. Interestingly, bio-SA-Fe/g-C_3N_4 exhibited outstanding reus-ability during the cyclic degradation of SMX and the degradation
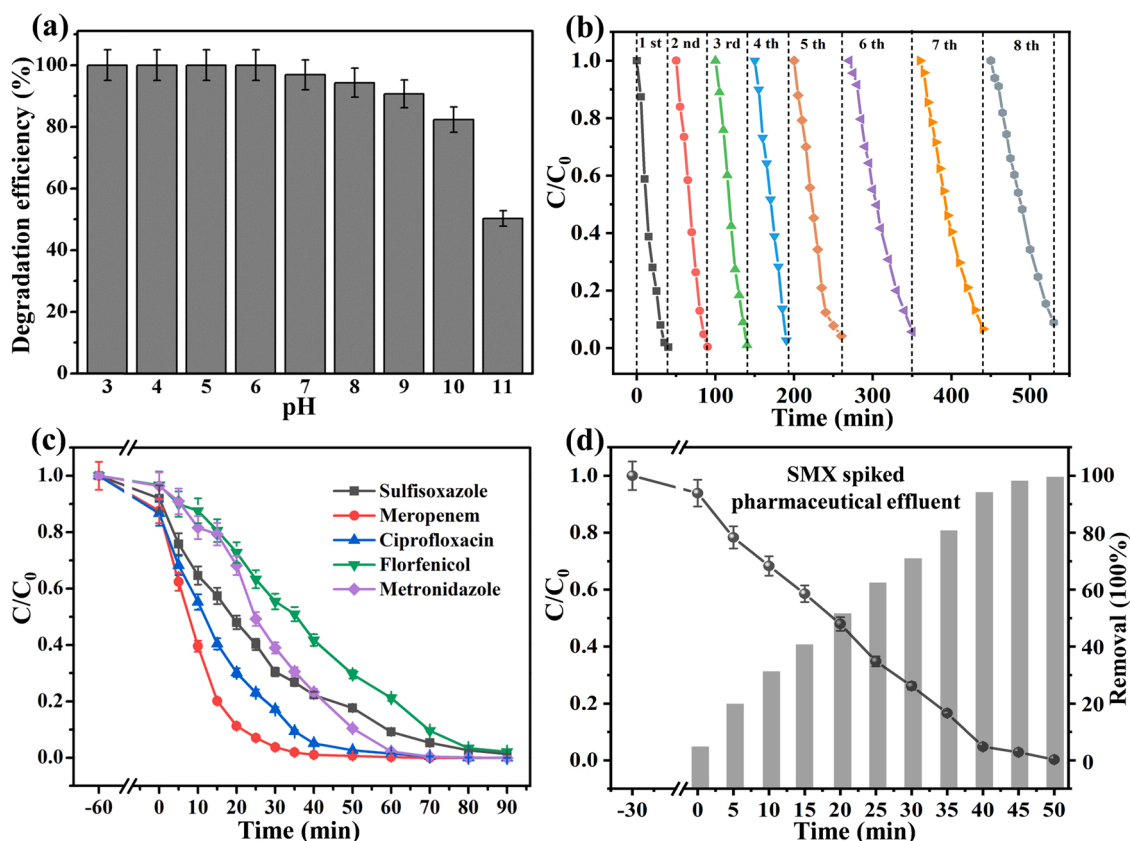
Fig. 2. (a) The effect of solution pH on the degradation of SMX and (b) cyclic degradation of SMX in the SA-Fe/g-C$_3$N$_4$ +H$_2$O$_2$ +Vis system. (c) Degradation of SIZ, MEM, CIP, FFC and MDZ; and (d) degradation of SMX spiked pharmaceutical effluent by the SA-Fe/g-C$_3$N$_4$ +H$_2$O$_2$ +Vis system. Reaction conditions: [SMX] = [SIZ] = [MEM] = [CIP] = [FFC] = [MDZ] = 20 mg/L, [H$_2$O$_2$] = 20 mM, [Catalyst] = 0.2 g/L, and pH = 3.0).

efficiencies maintained over 90% after eight cycles (Fig. 2b). Also, the bio-SA-Fe/g-C$_3$N$_4$ +H$_2$O$_2$ +Vis system was effective for the removal of other antibiotics (Fig. 2c), including SIZ, MEM, CIP, FFC and MDZ, and their removal efficiencies are ~98.5%, 100%, 100%, 97.8% and 100%, respectively. In addition, ~99% of SMX was eliminated from the spiked pharmaceutical effluent (Fig. 2d) and ~86.7% of the total organic carbon (TOC) (Fig. S8) was removed in the degradation systems, further implying the great application potential of the bio-SA-Fe/g-C$_3$N$_4$ for the treatment of antibiotic-containing wastewater.

Fig. S9 shows the degradation of SMX in the various systems. SMX degradation reaches ~3.8%, ~5.6% and ~18.7% in the H$_2$O$_2$ +Vis, g-C$_3$N$_4$ +H$_2$O$_2$ and bio-SA-Fe/g-C$_3$N$_4$ +H$_2$O$_2$ systems, respectively, indicating sole visible light or g-C$_3$N$_4$ was not able to activate H$_2$O$_2$ and bio-SA-Fe sites can directly catalyze the Fenton-like reaction. In addition, ~11.1% and ~32.8% of SMX were degraded in the g-C$_3$N$_4$ +Vis and bio-SA-Fe/g-C$_3$N$_4$ +Vis systems, respectively, suggesting the boosted photocatalytic performance by the embedded bio-SA-Fe sites. SMX removal was further accelerated in the coexistence of a photocatalyst, visible-light, and H$_2$O$_2$, reaching 45.4% in the g-C$_3$N$_4$ +H$_2$O$_2$ +Vis system and 99.6% in the bio-SA-Fe/g-C$_3$N$_4$ +H$_2$O$_2$ +Vis system. Therefore, the bio-SA-Fe sites played an important role in PFLR by synergistically accelerating photocatalysis and heterogeneous Fenton reaction, giving rise to the remarkably enhanced SMX degradation. The first-order kinetic model was established to investigate SMX degradation in the above systems and the corresponding kinetic parameters are listed in Table S3 [30]. As shown in Fig. 3a, the small kinetic rate constants (k) confirm the inefficient degradation of SMX in H$_2$O$_2$, Vis and H$_2$O$_2$ +Vis systems. As compared with the g-C$_3$N$_4$ +Vis and g-C$_3$N$_4$ +H$_2$O$_2$ systems (Figs. 3b and 3c), the bio-SA-Fe/g-C$_3$N$_4$ +Vis and bio-SA-Fe/g-C$_3$N$_4$ +H$_2$O$_2$ systems possess much larger k values for SMX degradation, verifying remarkably enhanced H$_2$O$_2$ activation and photocatalysis by the

bio-SA-Fe/g-C$_3$N$_4$ catalyst. In the bio-SA-Fe/g-C$_3$N$_4$ +H$_2$O$_2$ system (Fig. 3c), the first kinetic stage was much faster than the second kinetic stage, which could be due to the sluggish regeneration of Fe(II) species in the heterogeneous Fenton processes without light irradiation [31]. As shown in Fig. 3d, the second kinetic stage was significantly accelerated in the bio-SA-Fe/g-C$_3$N$_4$ +H$_2$O$_2$ +Vis system and the corresponding k_2 value was about ten-fold larger than that in the g-C$_3$N$_4$ +H$_2$O$_2$ +Vis system. This demonstrated the synergistic effect between photocatalysis and heterogeneous Fenton-like reactions mediated by the bio-SA-Fe sites in the bio-SA-Fe/g-C$_3$N$_4$ +H$_2$O$_2$ +Vis system.

3.3. Mechanisms for the enhanced photo-Fenton-like reactions

The optical properties of pristine g-C$_3$N$_4$ and bio-SA-Fe/g-C$_3$N$_4$ were studied by ultraviolet-visible diffuse reflectance spectra (UV-Vis DRS) and photoluminescence (PL) spectroscopy. From the UV-Vis DRS (Fig. 4a), it is seen that the pristine g-C$_3$N$_4$ can absorb solar light at a wavelength below 440 nm, which is in line with the optical bandgap of ~2.50 eV [32,33]. As compared with pristine g-C$_3$N$_4$, the optical absorption edge shifted to 700 nm for bio-SA-Fe/g-C$_3$N$_4$ and the direct band gap is narrowed down to ~1.1 eV (Fig. S11), indicating its enhanced abilities in producing photo-induced charge carriers. This is further evidenced by the color change from light yellow of g-C$_3$N$_4$ to brown of bio-SA-Fe/g-C$_3$N$_4$ (Fig. 4a). The bio-SA-Fe dopants may create impurity energy levels above the valence band (VB) edge of g-C$_3$N$_4$, and thus decrease the involved transition energy of photoexcited electrons [34]. From the PL spectra (Fig. 4b), the emission characteristics of bio-SA-Fe/g-C$_3$N$_4$ are similar to that of g-C$_3$N$_4$, but with a significant decrease in PL intensity. This is attributed to the implanted heteroatoms into the π-conjugated system of g-C$_3$N$_4$, which accelerates the mobility of charge carriers and restrains their recombination [35]. As can be seen
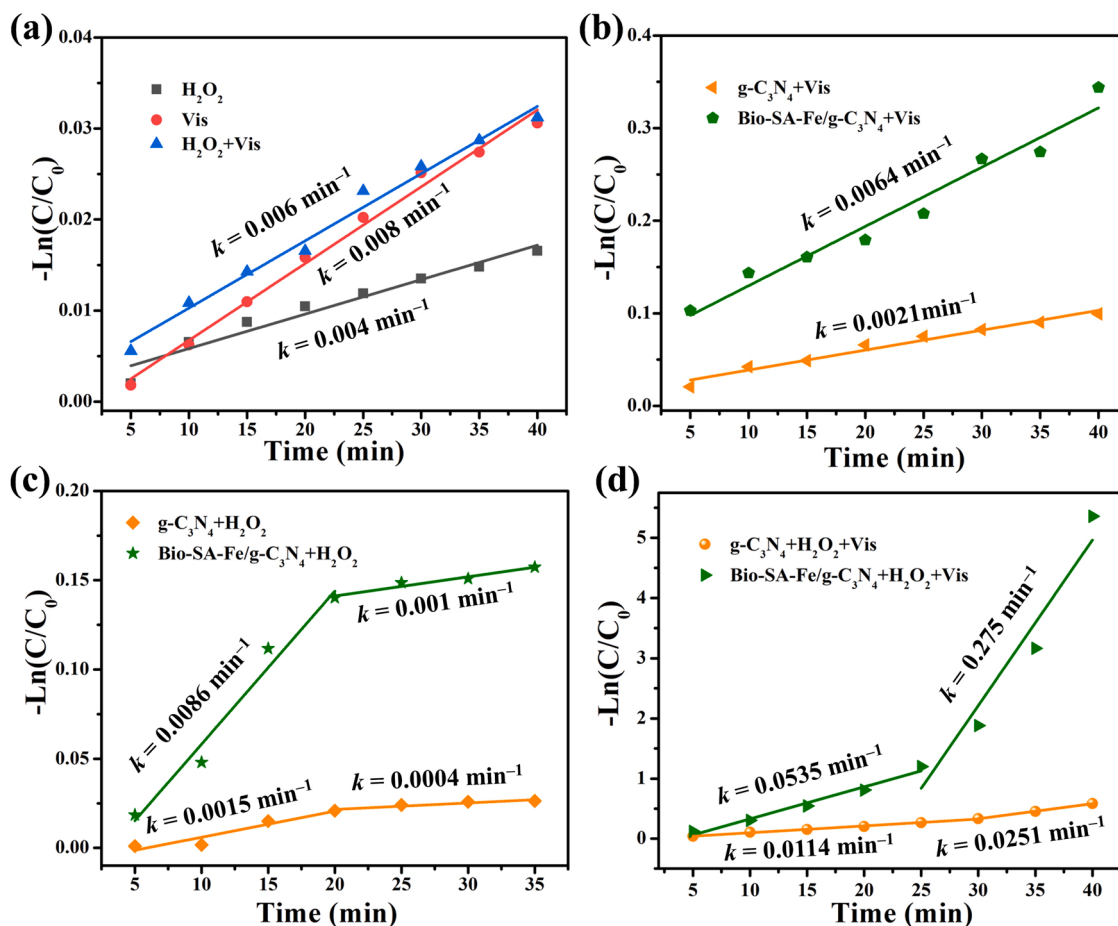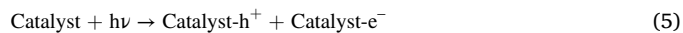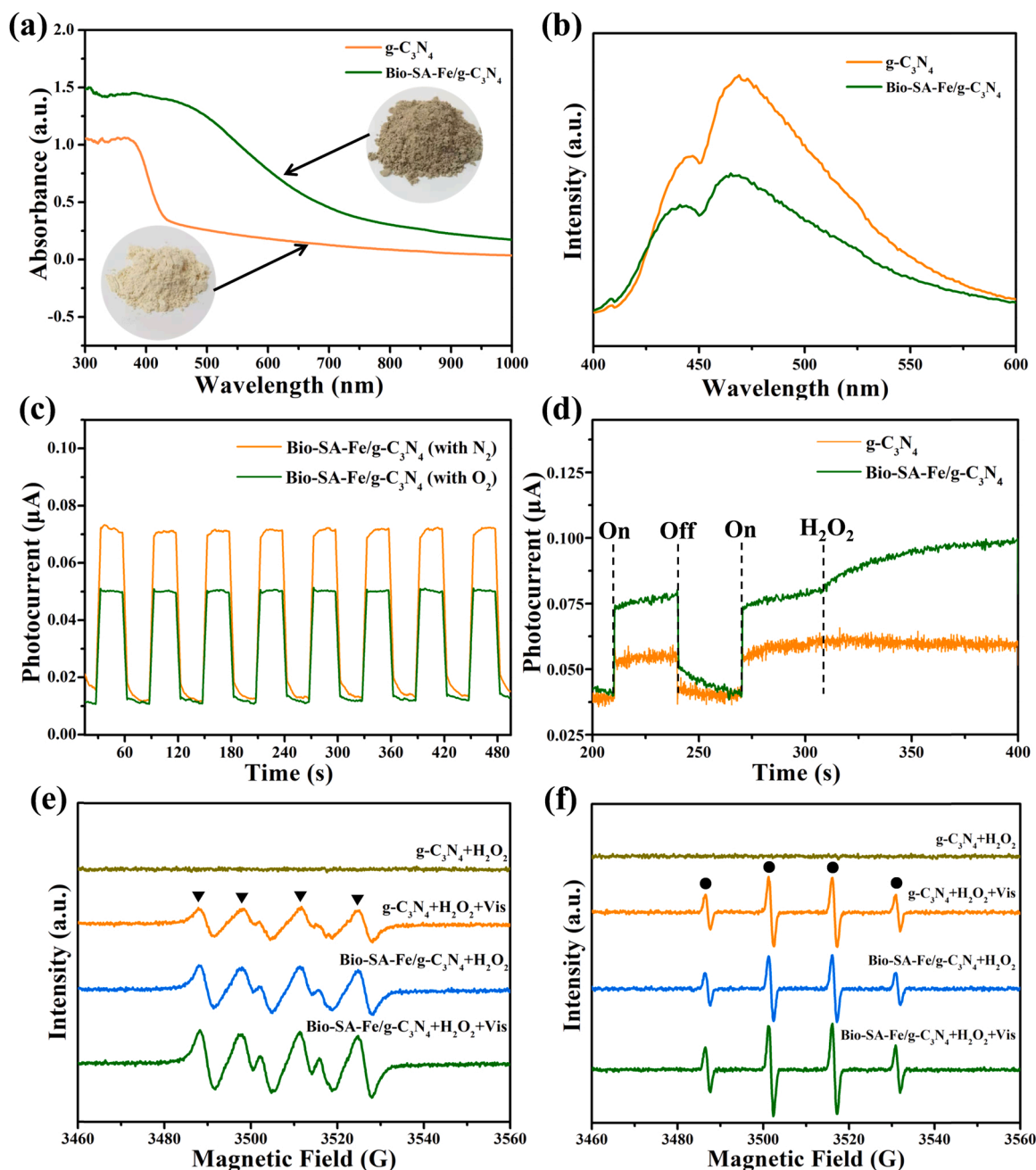
Fig. 3. Pseudo-first order kinetic plots for SMX degradation in the various systems. (a) H_2O_2, Vis and H_2O_2 +Vis systems, (b) g-C_3N_4 +Vis and bio-SA-Fe/g-C_3N_4 +Vis systems, (c) g-C_3N_4 +H_2O_2 and bio-SA-Fe/g-C_3N_4 +H_2O_2 systems, and (d) g-C_3N_4 +H_2O_2 +Vis and bio-SA-Fe/g-C_3N_4 +H_2O_2 +Vis systems (Reaction conditions: [SMX] = 20 mg/L, [H_2O_2] = 20 mM, [Catalyst] = 0.2 g/L and pH = 3.0).

from Fig. S10a, the photocurrent responses of bio-SA-Fe/g-C_3N_4 are much stronger than those of pristine g-C_3N_4, confirming the enhanced production, separation, and transportation of the photoinduced charge carriers. As compared with g-C_3N_4, bio-SA-Fe/g-C_3N_4 possesses a smaller arc radius in the electrochemical impedance spectroscopy (EIS) Nyquist plots, which confirms its lower interfacial charge transfer resistance (Fig. S10b). The charge transfer in the bio-SA-Fe/g-C_3N_4 +H_2O_2 +Vis system was monitored by photocurrent tests. As can be seen from Fig. 4c, the photocurrent intensity was decreased with O_2 bubbling, suggesting the efficient reduction of dissolved O_2 by photogenerated electrons (Eqs. 5 and 6). An enhanced photocurrent response of bio-SA-Fe/g-C_3N_4 was immediately observed after adding H_2O_2 (Fig. 4d). This phenomenon could be due to the fact that H_2O_2, as a hole scavenger [36], could capture the photogenerated holes and facilitated the separation of the electron-hole pairs.

The reactive species were identified by the electron paramagnetic resonance (EPR) spectroscopy. Fig. 4e depicts four characteristic peaks for DMPO-$O_2^{\bullet-}$ in the g-C_3N_4 +H_2O_2 +Vis and bio-SA-Fe/g-C_3N_4 +H_2O_2 +Vis systems, indicating that $O_2^{\bullet-}$ was mainly generated from photocatalytic reduction of dissolved O_2 (Eqs. 5 and 6) [37]. Interestingly, strong DMPO-$O_2^{\bullet-}$ signals were also found in the bio-SA-Fe/g-C_3N_4 +H_2O_2 system but not in the g-C_3N_4 +H_2O_2 system, indicating the bio-SA-Fe sites also contributed to the direct oxidation of H_2O_2 to produce $O_2^{\bullet-}$ as described by Eqs. 4 and 7 [38]. Similarly, the DMPO-$\bullet$OH signals were observed in the g-C_3N_4 +H_2O_2 +Vis, bio-SA-Fe/g-C_3N_4 +H_2O_2 and bio-SA-Fe/g-C_3N_4 +H_2O_2 +Vis systems, except for the g-C_3N_4 +H_2O_2 system (Fig. 4f), further confirming the enhanced activation of H_2O_2 by the bio-SA-Fe sites. Therefore, hydroxyl radical was

produced by both photocatalysis and heterogeneous Fenton reaction in the bio-SA-Fe/g-C_3N_4 +H_2O_2 +Vis system (Eqs. 3 and 8). Moreover, the XPS analysis revealed that the $\equiv Fe^{2+}$ species maintained a high percentage in the recycled bio-SA-Fe/g-C_3N_4 (Fig. S12), owing to the accelerated circulation of the $\equiv Fe^{3+}/\equiv Fe^{2+}$ pair by photogenerated electrons (Eq. 9). These results demonstrated the benefits of bio-SA-Fe sites in promoting ROS generation via bridging photocatalysis and heterogeneous Fenton reaction. On one hand, the embedded bio-SA-Fe sites were more efficient for H_2O_2 activation under visible light due to rapid regeneration of Fe(II) species by light-excited electrons from the surrounding g-C_3N_4 network. On the other hand, the locally polarized bio-SA-Fe sites facilitate the light absorption and separation of the electron/hole pairs, boosting photocatalytic performances of the bio-SA-Fe/g-C_3N_4. As a result, the synergies in photocatalysis and heterogeneous Fenton reaction induced by the bio-SA-Fe sites collaboratively contribute to the accelerated SMX degradation in the bio-SA-Fe/g-C_3N_4 +H_2O_2 +Vis system.

$$Catalyst + h\nu \rightarrow Catalyst\text{-}h^+ + Catalyst\text{-}e^- \tag{5}$$

$$O_2 + e^- \rightarrow O_2^{\bullet-} \tag{6}$$

$$HO_2\bullet \rightarrow O_2^{\bullet-} + H^+ \tag{7}$$

$$h^+ + H_2O \rightarrow \bullet OH + H^+ \tag{8}$$

$$\equiv Fe^{3+} + e^- \rightarrow \equiv Fe^{2+} \tag{9}$$

Fig. 4. (a) UV–vis DRS spectra (insets show the color of the samples), and (b) PL spectra of g-C_3N_4 and bio-SA-Fe/g-C_3N_4, (c) photocurrent response of bio-SA-Fe/g-C_3N_4 with O_2 or N_2 bubbling, and (d) photocurrent response of g-C_3N_4 and bio-SA-Fe/g-C_3N_4 with the presence of H_2O_2. DMPO spin-trapping EPR spectra for (e) $O_2^{\bullet-}$ and (f) $\bullet$OH in the various systems. ($\bullet$ represents DMPO–$\bullet$OH and $\blacktriangledown$ represents DMPO–$O_2^{\bullet-}$).

3.4. Catalytic activity of the bio-SA-Fe sites

The catalytic activity of bio-SA-Fe (pyrrole-type FeN$_4$) sites were compared with conventional single-atom Fe dopant (pyridine-type FeN$_4$) in g-C_3N_4 by experimental and theoretical studies. The Fe-doped g-C_3N_4 (Fe/g-C_3N_4) samples were prepared according to the previous studies by one-pot pyrolysis of mixture precursors of FeCl$_3$/dicyandiamide (DCD) [39] and FeCl$_3$/urea [40], respectively (details can be seen from **Text S4**, Supporting Information). The Fe content was controlled to be close to that of bio-SA-Fe/g-C_3N_4 (Table S4). As shown in Fig. 5a, the catalytic performances of these Fe/g-C_3N_4 catalysts are inferior to that of bio-SA-Fe/g-C_3N_4, which is further supported by the photocurrent response, EIS Nyquist plots, UV-Vis-DRS spectra and PL spectra (Fig. S10). As compared to the large amounts of Fe leaching from the

Fe/g-C_3N_4 samples (over 50%), the loss of Fe ions from bio-SA-Fe/g-C_3N_4 was negligible in the reaction solution (Table S5). Moreover, there is no obvious change in the XRD pattern of the recycled bio-SA-Fe/g-C_3N_4 sample (Fig. 1g). As compared with the recently reported single-atom Fe-doped g-C_3N_4 (pyridine-type FeN$_4$) and composites of g-C_3N_4 with Fe-based nanoparticles (Table S6), the bio-SA-Fe/g-C_3N_4 catalyst exhibited comparable or better performance for HFLR with low dosages of H_2O_2 and catalyst, even though these Fe NPs/g-C_3N_4 composites have much higher Fe-loading. These results further verified the high stability and catalytic activity of the bio-SA-Fe sites, which inherited from the strong complexations of the pyrrole-type FeN$_4$ sites as well as the conjugated structure bonded with the g-C_3N_4.

As compared with g-C_3N_4 and Fe/g-C_3N_4, the bio-SA-Fe/g-C_3N_4 possessed the strongest EPR signals (Fig. 5b), indicating the highest
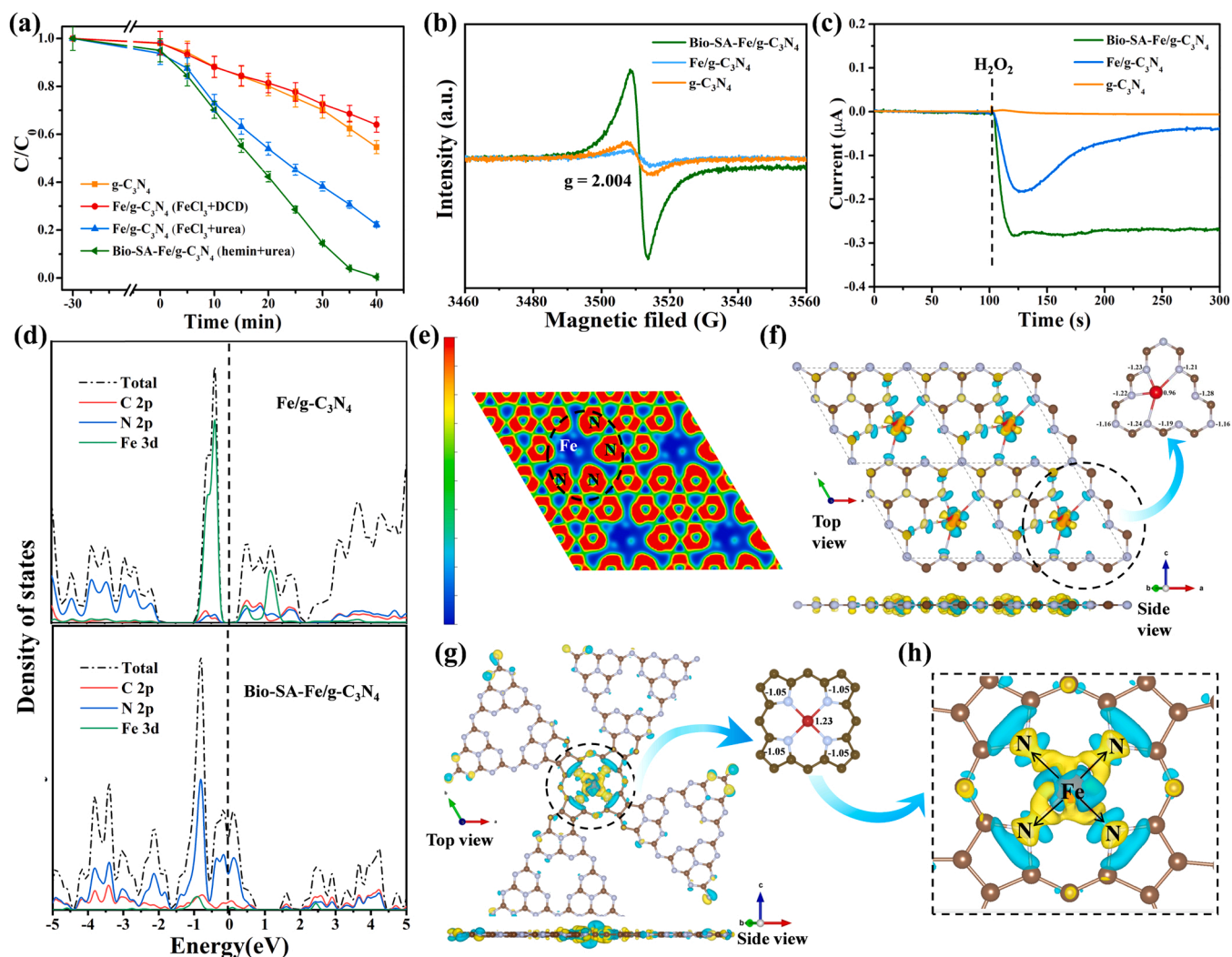
Fig. 5. (a) Catalytic degradation of SMX by g-C$_3$N$_4$, Fe/g-C$_3$N$_4$ and bio-SA-Fe/g-C$_3$N$_4$. (b) EPR spectra of the g-C$_3$N$_4$, Fe/g-C$_3$N$_4$ and bio-SA-Fe/g-C$_3$N$_4$. (c) *i–t* curves of the g-C$_3$N$_4$, Fe/g-C$_3$N$_4$ and bio-SA-Fe/g-C$_3$N$_4$ with the presence of H$_2$O$_2$. (d) PDOS of Fe/g-C$_3$N$_4$ and bio-SA-Fe/g-C$_3$N$_4$. (e) The electronic location function of the bio-SA-Fe/g-C$_3$N$_4$. Bader charge and differential charge distribution of (f) Fe-/g-C$_3$N$_4$ and (g, h) bio-SA-Fe/g-C$_3$N$_4$.

concentration of unpaired electrons in the bio-SA-Fe/g-C$_3$N$_4$ [41]. This is attributed to the doping of heme-like structure into the matrix of g-C$_3$N$_4$, resulting in the C-vacancies and creating more defect sites in the bio-SA-Fe/g-C$_3$N$_4$. These defect sites are beneficial to improving photocatalytic performance of the catalyst by promoting the separation of the photoexcited charge carries [42]. Besides the improved photocatalysis, as compared with g-C$_3$N$_4$ and Fe/g-C$_3$N$_4$, the bio-SA-Fe/g-C$_3$N$_4$ also exhibited an enhanced performance in a sustained and steady activation of H$_2$O$_2$ as observed from the *i-t* response (Fig. 5**c**). Theoretical calculations were applied to further compare the catalytic behaviors of the pyrrole-type bio-SA-Fe sites with the conventional pyridine-type FeN$_4$ sites doped in g-C$_3$N$_4$. From the DFT calculations (Fig. 5**d**), the partial density of states (PDOS) of Fe/g-C$_3$N$_4$ shows the presence of impurity bandgap located between the Fermi level and the valence band (VB), which is mainly contributed from the Fe 3d orbitals. The top of VB is dominated by N 2p orbitals and the botton of the conduction band (CB) is mainly contributed from the Fe 3d orbitals, suggesting the doped Fe in the Fe/g-C$_3$N$_4$ has changed the electronic structures of CB. For the bio-SA-Fe/g-C$_3$N$_4$, the VB and CB are both dominated by N 2p and C 2p orbitals, because of the strong delocalization of the conjugated pyrrole-type FeN$_4$ sites. The electronic location function (ELF) also reveals the stronger electrons' delocalization of the pyrrole-type FeN$_4$ sites (Fig. S13) than that of the pyridine-type FeN$_4$

sites in g-C$_3$N$_4$ matrix (Fig. 5**e**). The stronger Fe-N interaction of the bio-SA-Fe sites was also verified by the above EXAFS analysis, which facilitated the electron transfer between the Fe single sites and the g-C$_3$N$_4$ substrate [43]. Moreover, the VB of bio-SA-Fe/g-C$_3$N$_4$ evidently crossed the Fermi level and narrowed the band gap, which promotes the electron transition between the energy levels [44]. Thus, the tailored electronic structure endows the bio-SA-Fe/g-C$_3$N$_4$ with a higher carrier density and improved charge mobility [45]. Additionally, the Bader charge and differential charge distribution reveals the Fe single sites of bio-SA-Fe/g-C$_3$N$_4$ are more conducive to charge distribution as compared to that of the Fe dopant in g-C$_3$N$_4$ (Fig. 5**f-h**), leading to a faster electron transfer from g-C$_3$N$_4$ substrates to bio-SA-Fe active sites [45].

The energy profiles for the activation of H$_2$O$_2$ via the bio-SA-Fe sites and the Fe dopant in g-C$_3$N$_4$ were also evaluated by DFT calculations. The configurations of Model A (Fe-coordinated with four pyridinic N in the vacancy of g-C$_3$N$_4$ matrix for Fe/g-C$_3$N$_4$) and Model B (Fe coordinated four pyrrolic N in the porphyrin ring for bio-SA-Fe/g-C$_3$N$_4$) were constructed and their geometries were optimized (Fig. S14). The absolute energies (AE: a.u.) and relative energies (RE: kcal/mol) for H$_2$O$_2$ activation by Models A and B are listed in Table S7. Model B exhibits smaller absolute energy than Model A, suggesting that Model B is more stable than Model A. As shown in Fig. S13, activation of H$_2$O$_2$ mediated

by Model A is strongly endothermic (10.4 kcal/mol) with a high reaction barrier of 16.2 kcal/mol, which is thermodynamically unfavorable. By contrast, activation of H_2O_2 mediated by Model B is exothermic (15.2 kcal/mol) with a smaller reaction barrier (2.5 kcal/mol). Therefore, the theoretical calculations well support the experimental findings that the enzyme-mimicking bio-SA-Fe sites are more favorable for the homolytic cleavage of peroxide O−O bond in H_2O_2 to produce •OH [23, 46]. From the experimental and theoretical studies, we can conclude that the precisely regulated bio-SA-Fe sites are robust and efficient for the PFLR. This study provides new insights into the bio-inspired SACs for environmental remediation and implications for other heterogeneous redox reactions.

4. Conclusions

In conclusion, we have successfully fabricated enzyme-mimicking pyrrole-type FeN$_4$ single sites embedded in g-C$_3$N$_4$ by a facile copolymerization approach. The resultant strong π-conjugated system by coupling the pyrrole-type FeN$_4$ sites with the photocatalytic g-C$_3$N$_4$ substrate promoted the generation and transportation of the charge carriers as well as the redox circulation of the Fe sites. As a result, PFLR mediated by the bio-SA-Fe/g-C$_3$N$_4$ was dramatically boosted, leading to the efficient abatement of various antibiotics in wastewater. The results indicate $O_2^{\bullet-}$ and •OH radicals are the dominant reactive species for the degradation and mineralization of SMX and other antibiotics. Moreover, for the first time, we demonstrated that the bio-SA-Fe-N$_4$ sites were more stable and active than the conventional pyridine-type FeN$_4$ sites in g-C$_3$N$_4$ for PFLR by both experiments and computations. This study provides an example for synthesis of robust bio-inspired SACs and shed a new light of the application of the novel SACs in environmetal remediation.

CRediT authorship contribution statement

Shiang Liu: Data curation, Formal analysis, Writing & editing. **Dan Liu**: Methodology, Data curation, Formal analysis. **Yilang Sun**: Methodology, Data curation, Formal analysis. **Peiyuan Xiao**: Methodology, Data curation, Formal analysis. **Hongjun Lin**: Investigation, Funding acquisition. **Jianrong Chen**: Methodology, Investigation, Funding acquisition. **Xi-Lin Wu**: Writing - review & editing, Supervision. **Xiaoguang Duan**: Writing - review & editing, Supervision. **Shaobin Wang**: Editing, Supervision.

Declaration of Competing Interest

The authors declare that they have no known competing financial interests or personal relationships that could have appeared to influence the work reported in this paper.

Appendix A. Supporting information

Supplementary data associated with this article can be found in the online version at doi:10.1016/j.apcatb.2022.121327.

References

[1] I.N. Dias, B.S. Souza, J.H.O.S. Pereira, F.C. Moreira, M. Dezotti, R.A.R. Boaventura, V.J.P. Vilar, Chem. Eng. J. 247 (2014) 302–313.
[2] E.A. Serna-Galvis, J. Silva-Agredo, A.L. Giraldo, O.A. Flórez-Acosta, R.A. Torres-Palma, Sci. Total Environ. 541 (2016) 1431–1438.
[3] F. Chen, X.L. Wu, C. Shi, H. Lin, J. Chen, Y. Shi, S. Wang, X. Duan, Adv. Funct. Mater. 31 (2021) 2007877.
[4] C. Guo, C. Chen, J. Lu, D. Fu, C.-Z. Yuan, X.-L. Wu, K.N. Hui, J. Chen, J. Colloid Interface Sci. 599 (2021) 219–226.
[5] J. Lu, C. Chen, M. Qian, P. Xiao, P. Ge, C. Shen, X.L. Wu, J. Chen, J. Colloid Interface Sci. 603 (2021) 856–863.
[6] O. Legrini, E. Oliveros, A.M. Braun, Chem. Rev. 93 (1993) 671–698.
[7] Y. Zhu, R. Zhu, Y. Xi, J. Zhu, G. Zhu, H. He, Appl. Catal. B Environ. 255 (2019), 117739.
[8] M. Munoz, Z.M. de Pedro, J.A. Casas, J.J. Rodriguez, Appl. Catal. B Environ. 176–177 (2015) 249–265.
[9] A.V. Vorontsov, J. Hazard. Mater. 372 (2019) 103–112.
[10] W. Zhang, W. Zheng, Adv. Funct. Mater. 26 (2016) 2988–2993.
[11] H. Zhang, G. Liu, L. Shi, J. Ye, Adv. Energy Mater. 8 (2018), 1701343.
[12] N. Kong, X. Fan, F. Liu, L. Wang, H. Lin, Y. Li, S.-T. Lee, ACS Nano 14 (2020) 5772–5779.
[13] Z. Liu, S. Li, J. Yang, X. Tan, C. Yu, C. Zhao, X. Han, H. Huang, G. Wan, Y. Liu, K. Tschulik, J. Qiu, ACS Nano 14 (2020) 11662–11669.
[14] J. Chen, Q. Wang, L. Huang, H. Zhang, K. Rong, H. Zhang, S. Dong, Nano Res. 11 (2018) 4905–4913.
[15] H. Lan, Y. Tang, X. Zhang, S. You, Q. Tang, X. An, H. Liu, J. Qu, Chem. Eng. J. 345 (2018) 138–146.
[16] G. Kresse, J. Furthmüller, Comput. Mater. Sci. 6 (1996) 15–50.
[17] P.E. Blochl, Phys. Rev. B 50 (1994) 17953–17979.
[18] J.P. Perdew, K. Burke, M. Ernzerhof, Phys. Rev. Lett. 77 (1996) 3865–3868.
[19] R. Santucci, F. Sinibaldi, P. Cozza, F. Polticelli, L. Fiorucci, Int. J. Biol. Macromol. 136 (2019) 1237–1246.
[20] Z.-A. Lan, G. Zhang, X. Wang, Appl. Catal. B Environ. 192 (2016) 116–125.
[21] H. Wang, X. Yuan, H. Wang, X. Chen, Z. Wu, L. Jiang, W. Xiong, G. Zeng, Appl. Catal. B Environ. 193 (2016) 36–46.
[22] X. Wang, Z. Nan, Sep. Purif. Technol. 233 (2020), 116023.
[23] L. Jiao, J. Wu, H. Zhong, Y. Zhang, W. Xu, Y. Wu, Y. Chen, H. Yan, Q. Zhang, W. Gu, L. Gu, S.P. Beckman, L. Huang, C. Zhu, ACS Catal. 10 (2020) 6422–6429.
[24] X. Ao, W. Zhang, Z. Li, J.G. Li, L. Soule, X. Huang, W.H. Chiang, H.M. Chen, C. Wang, M. Liu, X.C. Zeng, ACS Nano 13 (2019) 11853–11862.
[25] S. An, G. Zhang, T. Wang, W. Zhang, K. Li, C. Song, J.T. Miller, S. Miao, J. Wang, X. Guo, ACS Nano 12 (2018) 9441–9450.
[26] W. Liu, K. Wang, C. Wang, W. Liu, H. Pan, Y. Xiang, D. Qi, J. Jiang, J. Mater. Chem. A 6 (2018) 22851–22857.
[27] B. Qiao, J.-X. Liang, A. Wang, C.-Q. Xu, J. Li, T. Zhang, J.J. Liu, Nano Res. (2015) 2913–2924.
[28] T. Xu, R. Zhu, G. Zhu, J. Zhu, X. Liang, Y. Zhu, H. He, Appl. Catal. B Environ. 212 (2017) 50–58.
[29] A. Babuponnusami, K. Muthukumar, Chem. Eng. J. 183 (2012) 1–9.
[30] C. Shi, D. Fu, J. Wang, X.-L. Wu, J. Chen, Sci. Sin. Chim. 51 (2021) 1104–1112.
[31] P. Zhou, W. Ren, G. Nie, X. Li, X. Duan, Y. Zhang, S. Wang, Angew. Chem. Int. Ed. 59 (2020) 6517–16526.
[32] Y. Zheng, L. Lin, B. Wang, X. Wang, Angew. Chem. Int. Ed. 54 (2015) 12868–12884.
[33] Y. Hou, Y. Zhu, Y. Xu, X. Wang, Appl. Catal. B Environ. 156–157 (2014) 122–127.
[34] G. Liu, P. Niu, C. Sun, S.C. Smith, Z. Chen, G.Q. Lu, H.-M. Cheng, J. Am. Chem. Soc. 132 (2010) 11642–11648.
[35] G. Zhang, M. Zhang, X. Ye, X. Qiu, S. Lin, X. Wang, Adv. Mater. 26 (2013) 805–809.
[36] H. Dotan, K. Sivula, M. Grätzel, A. Rothschild, S.C. Warren, Energy Environ. Sci. 4 (2011) 958–964.
[37] W. Song, P. Ge, Q. Ke, Y. Sun, F. Chen, H. Wang, Y. Shi, X.L. Wu, H. Lin, J. Chen, C. Shen, Chemosphere 221 (2019) 166–174.
[38] D. Yuan, C. Zhang, S. Tang, X. Li, J. Tang, Y. Rao, Z. Wang, Q. Zhang, Water Res. 163 (2019), 114861.
[39] K. Li, Y. Liang, H. Yang, S. An, H. Shi, C. Song, X. Guo, Catal. Today 371 (2020) 58–63.
[40] Y. Peng, X. Yu, W. Yin, W. Dong, J. Peng, T. Wang, ACS Appl. Bio Mater. 3 (2019) 59–67.
[41] X. Mi, P. Wang, S. Xu, L. Su, H. Zhong, H. Wang, Y. Li, S. Zhan, Angew. Chem. Int. Ed. 60 (2021) 4588–4593.
[42] J. Liao, W. Cui, J. Li, J. Sheng, H. Wang, Xa Dong, P. Chen, G. Jiang, Z. Wang, F. Dong, Chem. Eng. J. 379 (2020), 122282.
[43] Q. Wu, W. Wei, X. Lv, Y. Wang, B. Huang, Y. Dai, J. Phys. Chem. C 123 (2019) 31043–31049.
[44] H. Su, W. Che, F. Tang, W. Cheng, X. Zhao, H. Zhang, Q. Liu, J. Phys. Chem. C 122 (2018) 21108–21114.
[45] X.H. Jiang, L.S. Zhang, H.Y. Liu, D.S. Wu, F.Y. Wu, L. Tian, L.L. Liu, J.P. Zou, S. L. Luo, B.B. Chen, Angew. Chem. Int. Ed. 59 (2020) 23112–23116.
[46] N. Jin, D.E. Lahaye, J.T. Groves, Inorg. Chem. 49 (2010) 11516–11524.